Article

DFT Investigations of Au$_n$ Nano-Clusters Supported on TiO$_2$ Nanotubes: Structures and Electronic Properties

Ying Wang and Ge Zhou *

College of Chemistry, Sichuan University, Chengdu 610064, China; wy091213zyx@163.com
* Correspondence: zhougekk@scu.edu.cn

Abstract: TiO$_2$ nanotubes (TiO$_2$NTs) are beneficial for photogenerated electron separation in photocatalysis. In order to improve the utilization rate of TiO$_2$NTs in the visible light region, an effective method is to use Au$_n$ cluster deposition-modified TiO$_2$NTs. It is of great significance to investigate the mechanism of Au$_n$ clusters supported on TiO$_2$NTs to strengthen its visible-light response. In this work, the structures, electronic properties, Mulliken atomic charge, density of states, band structure, and deformation density of Au$_n$ (n = 1, 8, 13) clusters supported on TiO$_2$NTs were investigated by DMOL3. Based on published research results, the most stable adsorption configurations of Au$_n$ (n = 1, 8, 13) clusters supported with TiO$_2$NTs were obtained. The adsorption energy increased as the number of Au adatoms increased linearly. The Au$_n$ clusters supported on TiO$_2$NTs carry a negative charge. The band gaps of the three most stable structures of each adsorption system decreased compared to TiO$_2$NTs; the valence top and the conduction bottom of the Fermi level come mainly from the contribution of 5d and 6s-Au. The electronic properties of the 5d and 6s impurity orbitals cause valence widening and band gap narrowing.

Keywords: DMOL3; TiO$_2$-nanotube; Au$_n$; geometries; electronic properties

1. Introduction

The research on nanostructure models of metal clusters supported on well-ordered metal oxide surfaces is significant, providing important insights into the properties and mechanisms of real catalyst systems, and thus has been conducted extensively over the past few years [1–13]. In these model systems, the nature and strength of the interaction between the metal clusters and the support materials not only govern the nucleation and stability of the metal clusters, but also control the geometric and electronic structure of the resulting cluster/oxide interface, which are in turn critical to the catalytic activity of oxide-supported metal clusters [1,2]. Titanium dioxide has attracted worldwide attention due to its potential applications in a wide variety of products, such as photocatalysis [14,15], solar cells [16–18], and designing nanostructure architectures [19–23], due to its excellent gas sensitivity, moisture sensitivity, dielectric effect, photoelectric conversion and photocatalytic properties, chemical stability, nontoxicity, and relatively low cost. Among the three different polymorphs of TiO$_2$, rutile, anatase, and brookite, the anatase phase has been extensively studied over the last few decades due to its technological applications and photocatalysis [24]. However, the low surface area (ca. 50 m^2/g) and the large band gap of TiO$_2$ (about 3.2 eV in the anatase phase [25]) limit its light absorption to only 5% of the solar spectrum [26–28], restricting its applications. In order to make more use of solar energy to increase the photocatalytic efficiency, it is more beneficial for absorbing visible light to reduce the band gap of TiO$_2$ and increase the surface area of TiO$_2$ materials. As is well known to us, among the nanostructures, namely simple assemblies of nanoparticles, one-dimensional (1D) nanostructures (nanorods, nanowires, and nanotubes) have a relatively large surface area. Accordingly, the TiO$_2$ nanotubes (TiO$_2$NTs) constructed by anatase are a promising structure with a large surface area of 328 m^2/g [29]. Furthermore, TiO$_2$NTs

have a smaller band gap than the bulk powders and strong adsorption capacity, which will be desired to improve the photocatalytic properties and photoelectricity conversion effects, and have attracted considerable attention. A 3D random network of nanoparticles with more particle boundaries is more beneficial for transporting charge carriers than 1D nanostructures. Therefore, the collection of photogenerated charge carriers should be enhanced for adopted 1D nanostructure materials [30–33].

Although the smaller band gap of TiO_2NTs was beneficial in the absorbing of visible lights [34], they clearly required more solar energy than modified nanotubes. In order to enhance the visible light sensitivity of TiO_2 photocatalyst materials, many efforts have been made. The main modification methods are the organic dye photosensitive process, noble metal deposition, metal ion doping, the semiconductor coupling method, and so on. Metal nanoparticles (NPs) have considerably better photostability than semiconductor quantum dots, which usually suffer from anodic corrosion [26,35,36]. Some metal elements such as Au, Pt, Ag, Cu, and Fe have been employed to tune the electronic structure and enhance the catalytic activity of TiO_2NTs [4,37–44]. Among various metal clusters, the Au cluster is considered as one of the most promising candidates owing to its high conductivity, good stability in the air, and controllability of the electrical properties. In contrast to the noble character of bulk Au, the Au cluster/metal oxide system (such as Au/TiO_2) has been extensively studied due to the unique catalytic activity of this system. Recently, Zhi and co-workers [37] demonstrated that an Au nanoparticle–TiO_2 nanotube junction was formed by using bovine serum albumin as a biotemplate, with the Au nanoparticles formed in the tube channels and even in the space between the tube bottom and the Ti substrate, which show highly improved electrochemical conductivity and act as electrode materials to achieve the enhanced direct electrochemistry of heme proteins. Shao et al. [38] reported plasmonic Au particles loaded on anodic TiO_2 nanotube films exhibiting about 145% enhancement of the photocurrent and 37% reduction in response time. Chen et al. [39] synthesized the TiO_2 nanotube-supported Pt/Au nanoparticles by means of the photo-assisted deposition approach. The studies have shown that TiO_2NT-supported Pt/Au nanoparticles exhibit very high electrocatalytic activity toward formic acid oxidation when the Au composition is between 30% and 50%. Zhao et al. [4] prepared Au (or Pt) loaded on TiO_2 nanotubes by means of the photo-deposition method for the degradation of methyl orange. The Au-loaded sample with an adsorption peak in the visible range becomes a visible light photocatalyst. In addition, other researchers [40–44] combined Au nanoparticles with other metal-loaded TiO_2NTs to achieve high catalytic performance.

For Au nanoparticles supported on TiO_2 nanotube systems, numerous investigations have been performed through many experiments. By contrast, the theoretical research providing important insights into the properties and mechanisms of real catalyst systems is scarce and significant. The purpose of this work is to investigation the micromechanisms of energy and charge transport in the nano-junction consisting of TiO_2NTs and Au_n clusters by building a nanostructure catalyst model. In this work, we report our results of first principles DFT calculation of Au_n clusters supported on the anatase TiO_2NT surface. The TiO_2NTs were obtained by rolling up a TiO_2 (101) surface, which was prepared by cleaving anatase bulk TiO_2 perpendicular to the [1 0 1] direction. The anatase (101) surface was selected due to its thermodynamic stability [45–48]. In adsorption experiments, we adopted a single Au atom to test the adsorption sites of the TiO_2NT surface. For the catalytic performance of Au, nanoparticles were defined by three major factors: contact structure, support selection, and particle size [49]. The 3D conformations are better suited for adsorption on a surface and concomitant oxidation and reduction reactions compared with planar conformations [7,50]. The measurements of CO oxidation using the temperature-programmed reaction by A. Sanchez [51] showed that the smallest gold cluster that catalyzes the reaction is Au_8. Similar results were obtained by Hannu Häkkinen [52] and Bokwon Yoon [53]. Based on previous research [49–54], the adsorptive conformation of Au_8 biplanar was adopted in our study. Atomic clusters show both electronic and geometric magic numbers, and 13 is a common magic number for many transition-metal clusters, including Au [55,56].

For Au_n nanoclusters with 11 to 14 atoms, there appears to be a transition from 2D to 3D structures [57]. The work of J. Oviedo suggested that the most stable structure of Au_{13} comprises face-centered cubes or icosahedrons [55]. Ghazal Shafai et al. [57] selected the lowest-energy isomers for four types of cluster: planar, flake, cuboctahedron, and icosahedrons. The results show that there is no energy barrier between the icosahedron and the cuboctahedron configurations. Under the principle of three-dimensional configuration, we adopted a face-centered cubic and icosahedron structure for the original structures of the Au_{13} cluster. After optimization, the icosahedrons deformed into a distorted face-centered cubic structure, which is consistent with results of [57]. Therefore, we used a cuboctahedron as the initial configuration of the Au_{13} cluster. After the geometric optimization without symmetry being restricted, an energy-stable Au_{13} cuboctahedral structure was obtained. In order to understand the driving mechanism that determines the morphology and charge transport of TiO_2NT-supported Au_n nanoparticles, the structural and electronic properties of the adsorption systems were studied.

2. Methodology

The geometric structures of the bare nanotube and bare Au_n clusters are shown in Figure 1. All the calculations were performed using the semi-core pseudopotential method within the DFT framework. Exchange and correlation terms were considered within the generalized gradient approximation (GGA) with a Perdew–Burke–Ernzerof (PBE) functional [58], the all-electron double numerical basis set with a polarized function (DNP), as implemented in Dmol3 code [59,60]. A tetragonal supercell with the size of 40 Å × 40 Å × c Å was set, where the parameter c was 11 Å, equal to the minimum periodic unit length of the TiO_2NT (6,0). The supercell included 32 titanium and 64 oxygen atoms with the crystal form of $(TiO_2)_{32}$. The Brillouin zone was sampled by 4*4*2 [61] special k-points using the Monkhorst Pack [62] scheme for geometrical optimizations and the electronic properties calculation of TiO_2 anatase, TiO_2NT, and adsorption systems, respectively. A spin-restricted formalism was employed even in the presence of unpaired electrons, as the geometrical optimization is extremely sensitive to the details of the computational approach. The calculated bulk anatase TiO_2 lattice parameters ($a = b = 3.8283$ Å, $c = 9.5734$ Å, $u = 0.2080$ Å, where $u = d_{ap}/c$ is the internal coordinate and d_{ap} is the Ti-O top bond length) agree well with the experiments [25,63]. The calculated band gap of pure anatase TiO_2 is 2.77 eV, which is smaller than the experimental value, 3.2 eV [25]. This is due to the fact that density functional theory does not consider the electronic exchange-correlation potential discontinuity, which results in the basic band gap width being smaller than the experimental value by about 30–50%, generally. This does not affect the analysis of the electronic structure. The initial single-walled anatase TiO_2NT models were constructed by rolling up one (101) layer of the anatase structure in the $[\overline{1}01]$ direction [30,34,64,65]. The (101) layer has 12 atoms (four titanium and eight oxygen atoms) in the unit cell and with the basic vectors V and U in the [010] and $[\overline{1}01]$ directions, respectively. The nanotubes were obtained by rolling up the layer in ways in which the chiral vectors (6,0) = 6 V became the circumferences of the nanotube. The 1D line symmetry group of the nanotube TiO_2NT (6,0) can be represented as P42/mmc (D4H-9).

According to the work of Vittadini and Selloni on TiO_2 (101) surface adsorption of Au clusters [3], the adsorption energies for Au_n clusters are as follows:

$$E_{Au_n}^{ads} = -\left(E_{Au_n/TiO_2NT} - E_{TiO_2NT} - E_{Au_n}\right) \tag{1}$$

where E_{Au_n/TiO_2NT} (E_{TiO_2NT}) represents the energy of the nanotube with (without) the adsorbate, and E_{Au_n} denotes the energy of the gas-phase cluster.

We also define a cohesive energy to obtain information about the clustering energetics:

$$E_{Au_n}^{clu} = -\left(E_{Au_n/TiO_2NT} - E_{TiO_2NT} - nE_{Au}\right)/n \tag{2}$$

where E_{Au} is the total energy of a free Au atom. $E_{Au_n}^{ads} = E_{Au_n}^{clu}$, when a single Au adatom is on the TiO$_2$NT surface.
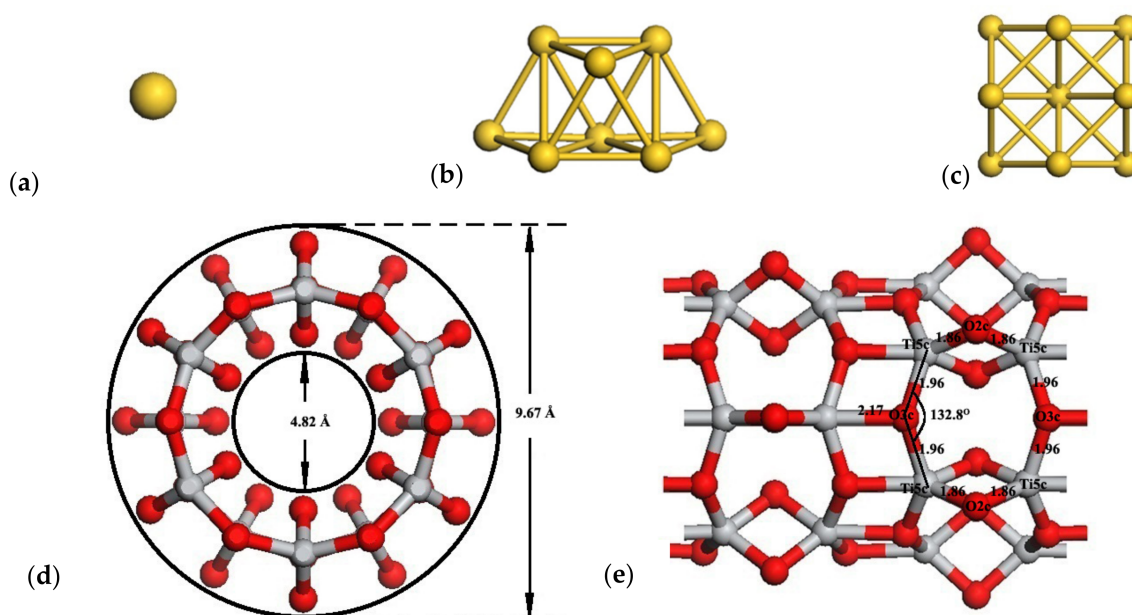

Figure 1. Optimized geometry of bare Au clusters and the bare TiO$_2$NT (6,0). The first three configurations are: (**a**) Au$_1$; (**b**) Au$_8$biplanar; (**c**) Au$_{13}$ cuboctahedral. (**d**,**e**) are the cross-sectional and the side view of the TiO$_2$NT (6,0), respectively. The gold atoms are shown in gold, the oxygen atoms are displayed in red, while titanium atoms are presented in light gray.

Electronic structure analyses, including Mulliken charge and density of states (DOS), the partial density of states (PDOS), as well as deformation density, energy gap, and molecular orbital, were performed with DMOL3 of Materials Studio package (MS, version 8.0 Accelrys Software Inc., San Diego, CA, USA). These analyses were used to help us understand the nature of bonding and the interaction between Au$_n$ clusters and anatase TiO$_2$NTs.

3. Results and Discussion

3.1. Structures of Anatase TiO$_2$ Nanotubes

The cross-sectional and side view of the optimized TiO$_2$NT (6,0) are shown in Figure 1. In the TiO$_2$NT (6,0), both the inner and outer walls were terminated with the two-fold-coordinated oxygen atoms (2cO). In addition to 2cO atoms, three-fold-coordinated oxygen atoms (3cO) as well as five-fold-coordinated (5cTi) atoms are also exposed on the surface of the TiO$_2$NT (6,0).

3.2. Structures of Au$_1$/TiO$_2$NTs

Two different stable adsorption structures were found for a single Au adatom on the TiO$_2$NT (6,0) surface, as shown in Figure 2: a symmetric bridging site between two edge 2cO atoms in the $[\bar{1}01]$ direction, Au$_{1(O,O)}$, and the other right on top of a 3cO atom, as well as bonding to three 5cTi atoms, Au$_{1(O,Ti)}$. The adsorption energies of Au in these two configurations are listed in Table 1. For the two stable configurations, the adsorption energy of Au$_{1(O,Ti)}$ is 0.49 eV. Au$_{1(O,Ti)}$ is significantly more stable than Au$_{1(O,O)}$, which has an adsorption energy of about 0.20 eV. To illustrate the charge of adsorbed clusters and the charge distributions of clusters and related TiO$_2$NT surface atoms, Mulliken charge analysis was employed. The Mulliken charges of Au and the nanotube surface atoms that directly associated with the Au adatom are shown in Table 1. Apparently, Au became negatively charged by receiving electrons in both configurations. Both types of O atoms binding to Au directly became less negative, and most 5cTi atoms became more positive, except for 5cTi^3,

which generally indicated the loss of electrons. This is consistent with Au adsorption on the anatase TiO_2 (101) surface [3].
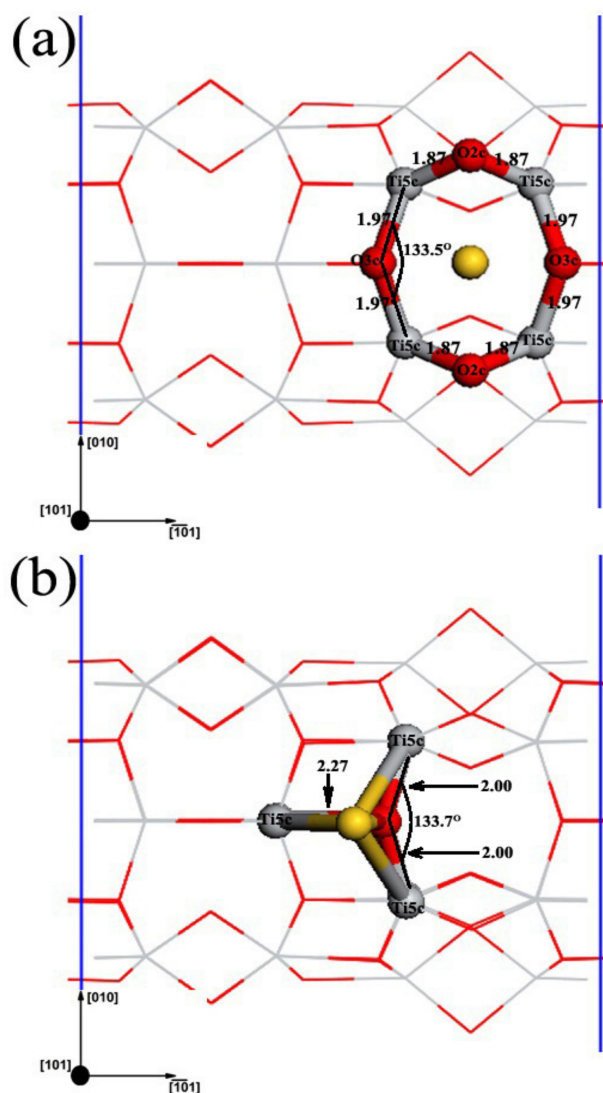

Figure 2. Top views of detailed adsorption structures for a single Au adatom on the TiO_2NT (6,0) surface: (**a**) $Au_{1(O,O)}$; (**b**) $Au_{1(O,Ti)}$.

Table 1. Adsorption and clustering energies of Au_1 and atomic Mulliken charges of Au and TiO_2NT surface atoms for the Au_1/TiO_2NT system in different configurations [a].

Configuration	Energy		Mulliken Charge (a.u.)							
	$E_{Au_1}^{ads}$ (eV)	Au	3cO [1]	2cO [1]	3cO [2]	2cO [2]	5cTi [1]	5cTi [2]	5cTi [3]
Bare TiO_2NT			−0.966	−0.779	−0.965	−0.779	1.714	1.714	1.713
$Au_{1(O,O)}$	0.20	−0.060	−0.958	−0.770	−0.958	−0.770			
$Au_{1(O,Ti)}$	0.49	−0.075			−0.940		1.732	1.731	1.676

[a] The superscripts on O and Ti indicate to which Au atom they are bounded.

The DOS plots of bare TiO_2NT and the adsorption system, and the PDOS plots of the Au adatom and the oxygen atoms and titanium atoms of TiO_2 nanotube, are shown in Figure 3 and are used to further illustrate bonding characteristics. For the projection of 2p orbitals of oxygen, 3d orbitals of titanium and 5d orbitals of gold showed the major contribution to the PDOS in the energy range of interest. Therefore, projections of individual

orbitals along with the DOS are shown. The zero on the energy axis of the plots corresponds to the Fermi level of the bare TiO_2NT and is at the top of the valence band, marked with a red dashed line in the figures. As presented in Figure 3a, the bare TiO_2NT is semiconducting, and the valence band mostly has a contribution by the O 2*p* orbital (red line in Figure 3a) with a small contribution from the Ti 3*d* orbital (blue line in Figure 3a). The conduction band is dominated by the Ti 3*d* orbital. The electron density contributed by the O 2*s* orbital in the low energy region from -0.8 Ha to -0.5 Ha has little effect on the electron structure regarding the Fermi level. Therefore, in the following parts, we do not discuss this any further. According to Figure 3b,c, after an Au atom was adsorbed on TiO_2NTs, the TiO_2NTs retained some semiconductor properties. The Fermi level moved close to the bottom of conduction band, and the valence band had mostly an O 2*p* character, but a new small peak of the Au 5*d* atom arose at the top of it. Correspondingly, a smaller peak of Au 6*s* appeared in the bottom of the conduction band at the zero of the energy axis. Compared with $Au_{1(O,O)}$, the Au 5*d* peak arose in the valence band separately. The valence band of $Au_{1(O,Ti)}$ contributed by the Au 5*d* peak, overlapped well with the O 2*p* and Ti 3*d*. It is thus more likely to cause electron transfer. The contribution of the Au 5*d* and 6*s* orbitals at the top valence band and bottom conduction band causes valence band broadening and band gap narrowing, which causes the adsorption band edge of TiO_2NTs to red shift.
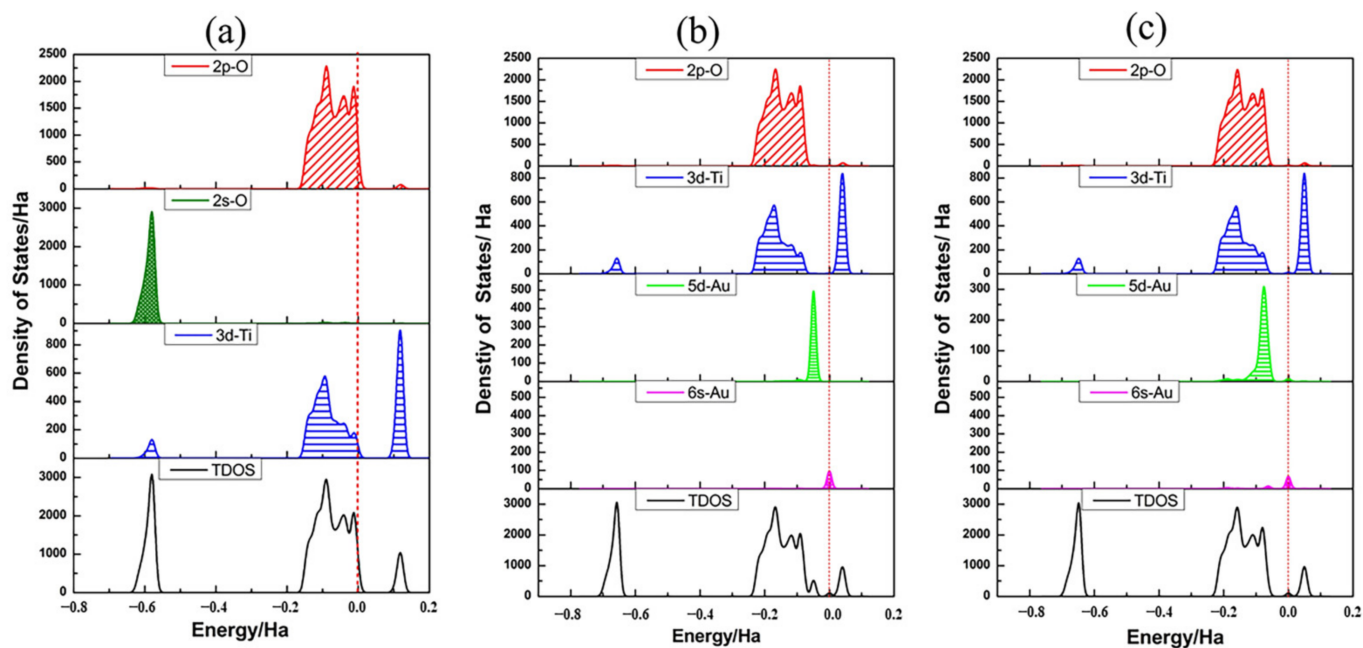

Figure 3. Density of state profiles and the partial density of states of TiO_2NT (6,0) and Au and relevant nanotube surface atoms for a single Au adatom in two different adsorption states: (**a**) bare TiO_2NT (6,0), (**b**) $Au_{1(O,O)}$, (**c**) $Au_{1(O,Ti)}$. The black curve is the sum of PDOS of O atoms, Ti atoms, and Au atoms from the optimized bare TiO_2NT (6,0)/Au systems, while the red curve indicates the 2*p* orbital of oxygen atoms, the dark green curve indicates the 2*s* orbital of oxygen atoms, the blue curve represents the 3*d* orbital of titanium atoms, the light green curve denotes the 5*d* orbital of gold atoms, and the magenta curve represents the 5*s* orbital of gold atoms, respectively. The Fermi level of bare TiO_2NTs is set at 0 eV, as denoted in the red dashed line.

The highest occupied molecular orbital (HOMO) and the lowest unoccupied molecular orbital (LUMO) along with the energy gap of bare TiO_2NTs and the adsorption system are shown in Figure 4. In the two adsorption configurations, the Au atoms are supported on the TiO_2NT surface, reducing the energy gap from 2.704 eV to 1.979 eV and 2.592 eV, respectively. Further analysis shows that the *d* orbital of Au adatoms has an evident contribution to the HOMO orbital. The results are the same as the previous analysis of DOS. This leads to the energy of HOMO ($Au_{1(O,O)}$) rising from -7.171 eV to -6.494 eV.

Meanwhile, the major feature of HOMO is that the Au 5*d* orbital as well as the O 2*p* orbital replaced the main contribution of O 2*p*. The energy of LUMO (Au$_{1(O,O)}$) decreases from −4.467 eV to −4.515 eV. The $3d_{x^2-y^2}$ orbital of Ti gives the contribution to the bottom of the conduction band. The character of the 6*s* orbital of Au was not obviously observed in the LUMO orbital.
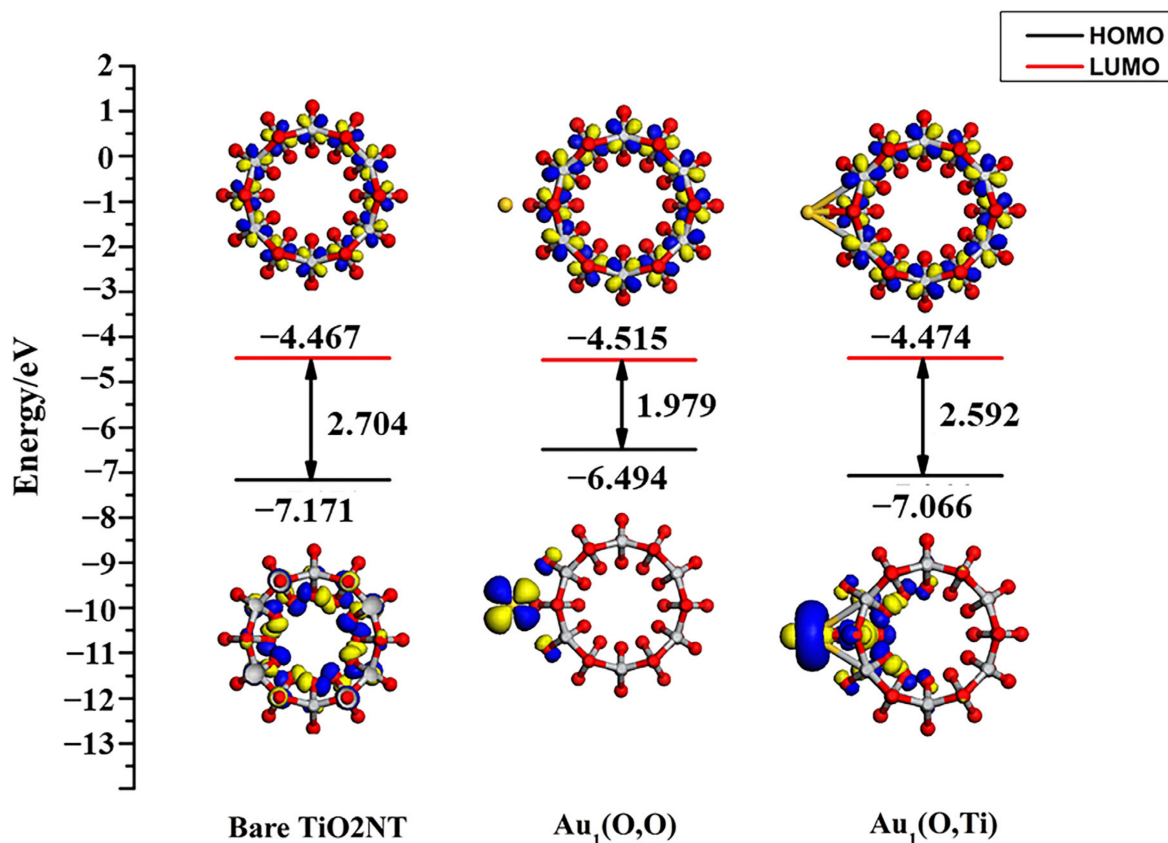

Figure 4. HOMO and LUMO along with the energy gap of bare TiO$_2$NT and two Au$_1$ adsorption systems calculated at the Γ-point. The isovalue set is 0.025 electrons/Å^3. The gold atoms are shown in gold, the oxygen atoms are displayed in red, while titanium atoms are presented in light gray. Blue and yellow regions represent the positive and negative parts of HOMO and LUMO respectively.

The bonding characteristics of the adsorption system are further demonstrated in the electron deformation density (EDD) contour maps in Figure 5. The EDD contour maps were defined as the total density by subtracting the isolated atoms' electron density. Compared with the Au$_{1(O,O)}$, which has no significant bonding between Au atoms, and 2cO atoms deposited on the TiO$_2$NT surface, the Au$_{1(O,Ti)}$ has an obvious depletion of electron density when the 3cO 2p orbital is aligned with the Au–3cO bond direction. Additionally, the Au atom was surrounded by a small number of electrons, which indicated the electron transfer from TiO$_2$NTs to gold nano-clusters.
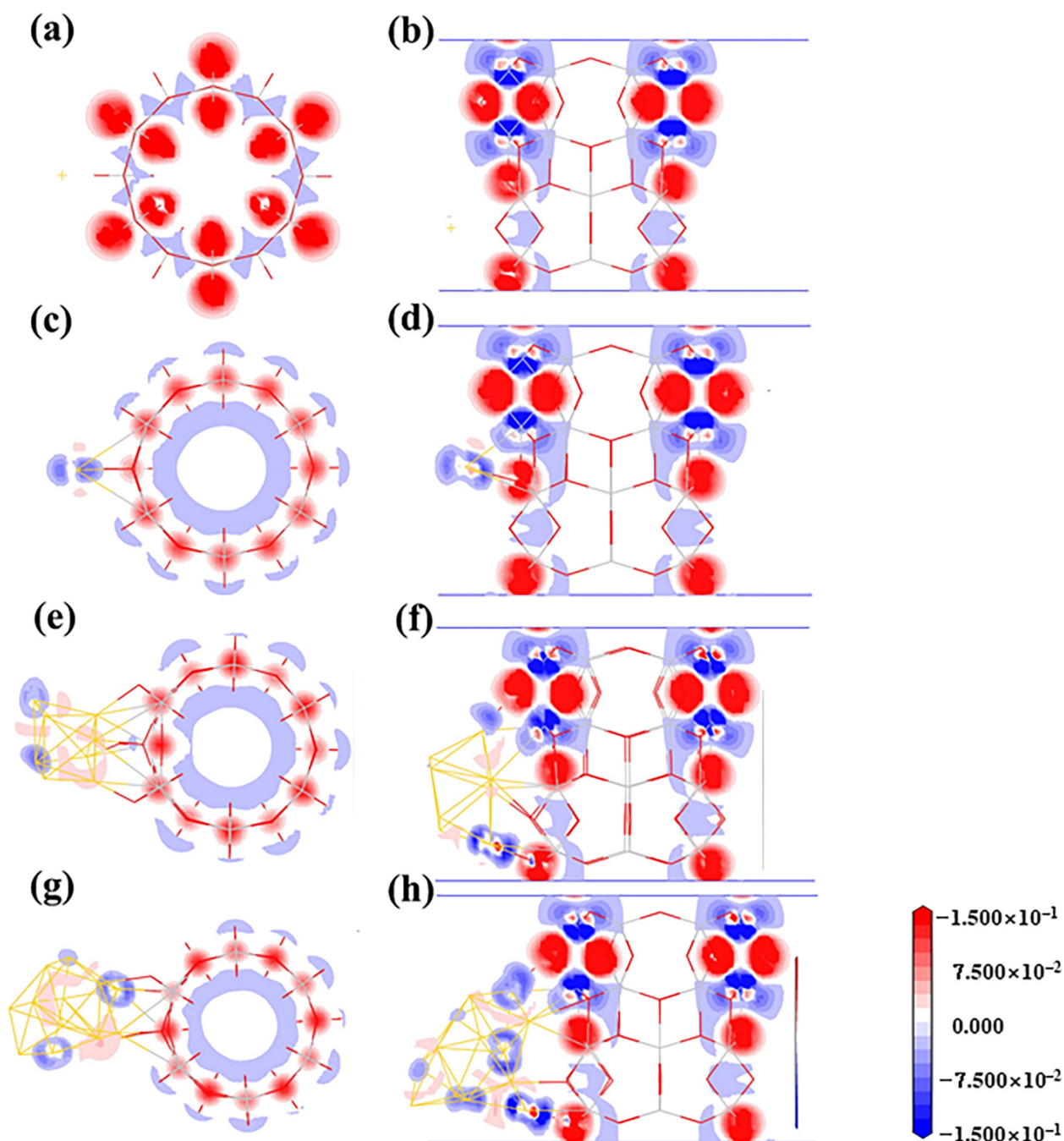
Figure 5. Deformation density contour maps for the adsorption of Au_n clusters on the TiO_2NT (6,0) surface. The configurations are as follows: (**a**,**c**,**e**,**g**) are the cross-sectional views of $Au_{1(O,O)}$, $Au_{1(O,Ti)}$, Au_{8-C}, and Au_{13-B}, respectively; (**b**,**d**,**f**,**h**) are the side views of $Au_{1(O,O)}$, $Au_{1(O,Ti)}$, Au_{8-C}, and Au_{13-B}, respectively. Contour level is −0.015~0.015 au. In this plot, a loss of electrons is indicated in blue, while electron enrichment is indicated in red.

3.3. Structures of Au₈/TiO₂NT

Figure 6 shows four different configurations of Au_8 clusters adsorbed on the TiO_2NT surface. The structures of Au_8 in the four adsorption systems still maintain the biplanar conformation. The adsorption energy and Mulliken charge analysis for all these structures are listed in Table 2. $Au_{8-A(2cO,3cO,2cO)}$ is the most stable configuration for the Au_8/TiO_2NT systems, as shown in Figure 6(A-a,A-b). In this structure, three Au atoms as an adsorption layer bond to TiO_2NT surface atoms, and the oxygen atoms of the TiO_2NT surface which

interacted with the Au_{8-A} were 2cO, 3cO, and 2cO, respectively. In the structure shown in Figure 6(B-a,B-b), $Au_{8-B(2cO,5cTi)}$ has an adsorption energy of about 0.86 eV, slightly smaller than Au_{8-A}, which has an adsorption energy of 1.11 eV. For the adsorption configuration of Au_{8-B}, similar to Au_{8-A}, there was an adsorption layer consisting of three Au atoms from the side direction of original Au_8 biplanar binding to the TiO_2NT directly. The third structure, $Au_{8-C(2cO,2cO,3cO)}$, which is displayed in Figure 6(C-a,C-b), is almost as stable as Au_{8-B}. The energy difference between the two structures is merely 0.05 eV. In Au_{8-C}, the adsorption layer is made up by four Au atoms as the bottom layer connecting with the TiO_2NT surface. Both the bottom and top layer are part of the rhombus. The fourth structure, $Au_{8-D(2cO,2cO,3cO)}$, is a result of the relaxation by five Au atoms of Au_8 biplanar parallel to the axial of TiO_2NTs. Au_{8-D}, as a local minimum, has similar binding sites to Au_{8-C}, and is evidently less stable than the three previous structures. Noticeably, the adsorption of Au adatoms caused the TiO_2NT surface's deformation; the 3cO atoms which bonded with Au adatoms were pulled off of the surface of TiO_2NT. Meanwhile, the other 3cO atoms which have no relation with the Au_8 clusters were "pushed" into a slightly concave formation. This phenomenon can be found in Figure 6. According to Table 2, the Au_8 clusters in four structures were negatively charged. Based on analysis of Au nanocluster size with Mulliken atomic charge and adsorption energy, for Au_8 clusters, not only transfer charges but also adsorption energies were increased, with clusters enlarging. Compared to Au_1 absorption systems with a charge of about −0.060 au and −0.075 au, respectively, there was a remarkable increase in the electron transfer to Au_8 clusters. The maximum charge is −0.424 au for the Au_{8-C} structure. This phenomenon suggested that more charge transfer will be required to enlarge the size of Au_n nanoclusters to a certain degree. The interatomic charge distributions of related TiO_2NT surface atoms were analyzed in detail. Apart from a few TiO_2NT surface atoms, there are two main trends in atomic charge redistribution after the adsorption of Au_8 clusters: electron transfer to oxygen atoms, and titanium losing electrons and showing greater positive charge.

PDOSs of Au_8 clusters as well as the associated TiO_2NT surface atoms in all four adsorption structures are plotted in Figure 7. The mixing between the O 2*p* orbital and Au 5*d*6*s* states spans the whole energy range of the valence band. Compared with the PDOS of a single Au adatom, the intensity of Au_8 clusters at the Fermi level was greatly increased. The Au clusters' 6*s* states make a dominating contribution to the states for the gap and are closely related to the Fermi level. The fact is that the energy gap of bare TiO_2NTs almost disappears in all four adsorption systems. This indicates that metallization of the nanojunction Au_8-TiO_2NT system occurs, and therefore further increases tunnelling currents [66].

For more detailed analysis, the molecular orbital diagrams of HOMO and LUMO along with band gaps of the adsorption systems are shown in Figure 8. As the Au_8 clusters adsorb on the TiO_2NT surface, the contribution of metal clusters to the HOMO and the LUMO of the Fermi level is increased. As in the analysis of DOS, the band gap of the Au_8–TiO_2NT nanojunction was below 1.10 eV; Au_8 clusters narrowed the band gap of the system more efficaciously than a single Au adatom. From the EDD contour maps of the Au_8 adsorption system in Figure 5e,f, it can be found that Au_8 clusters obtained electrons from TiO_2NTs. In addition to the electron cloud distribution in Au_8 nanoclusters, the Au atoms which have direct bonding with TiO_2NT surface atoms show obvious electron accumulation, such as a Au_{8-C} structure, as shown in Figure 5f.
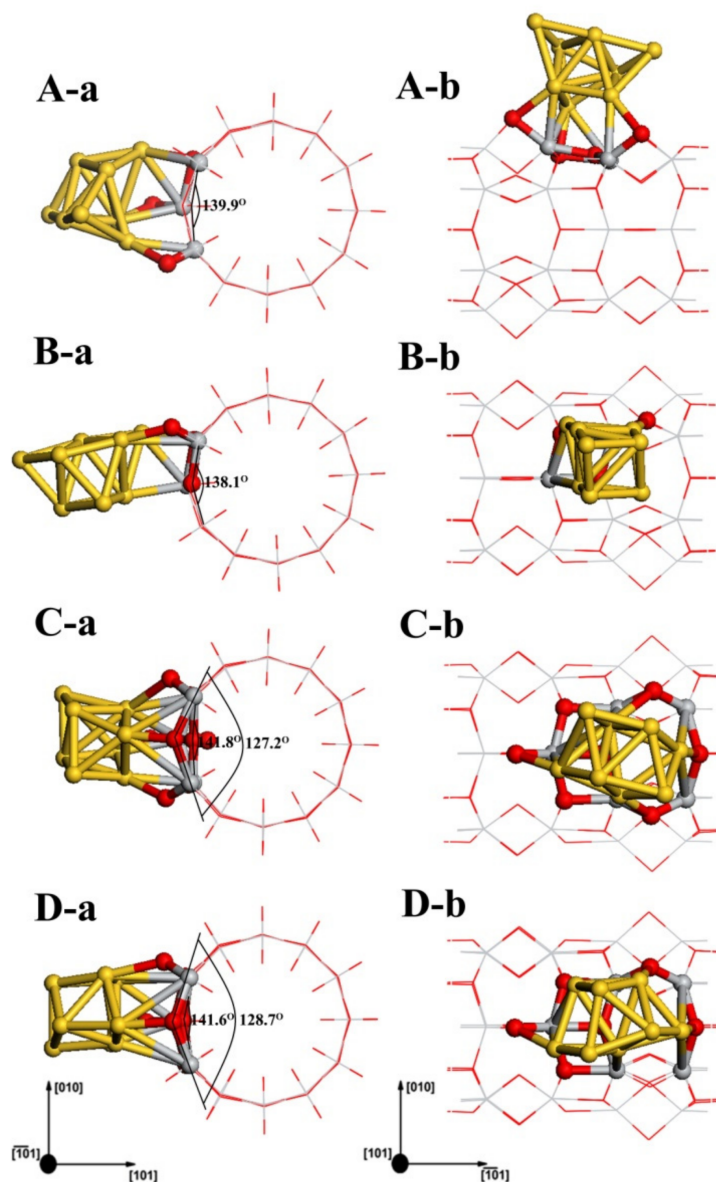
Figure 6. Four adsorption geometries for Au$_8$ clusters on the TiO$_2$NT (6,0) are displayed as (**A–D**). (**a,b**) depict the cross-sectional view and the side view of the Au$_8$ cluster absorption systems, respectively. The cross-sectional views of four adsorption geometries are shown as (**A-a,B-a,C-a,D-a**), respectively. The side vies of four adsorption geometries are shown as (**A-b,B-b,C-b,D-b**), respectively.

Table 2. Adsorption and clustering energies of Au$_8$ and atomic Mulliken charges of Au and TiO$_2$NT surface atoms for the Au$_8$/TiO$_2$NT system in different configurations [a].

Configuration	Energy			Mulliken Charge (a.u.)									
	$E_{Au_8}^{ads}$ (eV)	$E_{Au_8}^{clu}$ (eV/atom)	Au$_8$	3cO [1]	2cO [1]	2cO [2]	3cO [2]	2cO [3]	5cTi [1]	5cTi [2]	5cTi [3]	5cTi [4]	5cTi [5]
Bare TiO$_2$NT				−0.966	−0.779	−0.779	−0.966	−0.779	1.717	1.714	1.718	1.714	1.713
Au$_{8-A(2cO, 3cO, 2cO)}$	1.11	2.12	−0.321		−0.836		−0.965	−0.809	1.720	1.834		1.766	1.892
Au$_{8-B(2cO,5cTi)}$	0.86	2.09	−0.293			−0.851	−0.960					1.815	1.803
Au$_{8-C(2cO,2cO,3cO)}$	0.81	2.09	−0.424	−0.993	−0.826	−0.758		−0.843	1.926	1.874	1.716	1.783	1.905
Au$_{8-D(2cO,2cO,3cO)}$	0.72	2.07	−0.343	−0.987		−0.818		−0.817	1.733	1.769	1.751	1.783	1.870

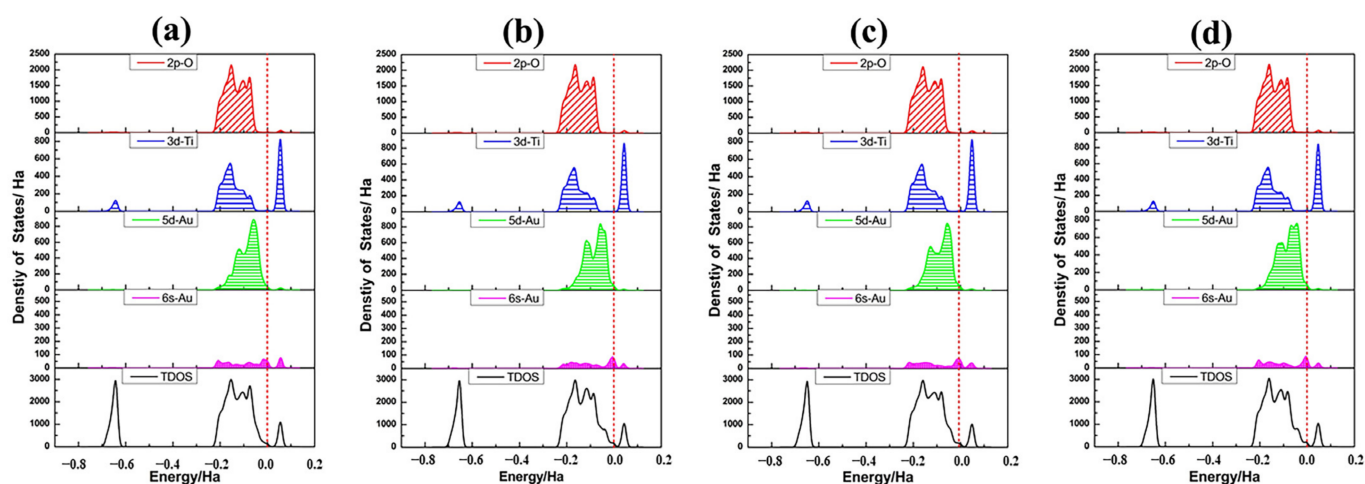[a] The superscripts on O and Ti indicate to which Au atom they are bound.

Figure 7. Density of state profiles and the partial density of states of Au_8 and relevant nanotube surface atoms for Au_8 clusters in four different adsorption states: (**a**) $Au_{8-A(2cO,3cO,2cO)}$; (**b**) $Au_{8-B(2cO,5cTi)}$; (**c**) $Au_{8-C(2cO,2cO,3cO)}$; (**d**) $Au_{8-D(2cO,2cO,3cO)}$. The detailed information is same as in Figure 3.
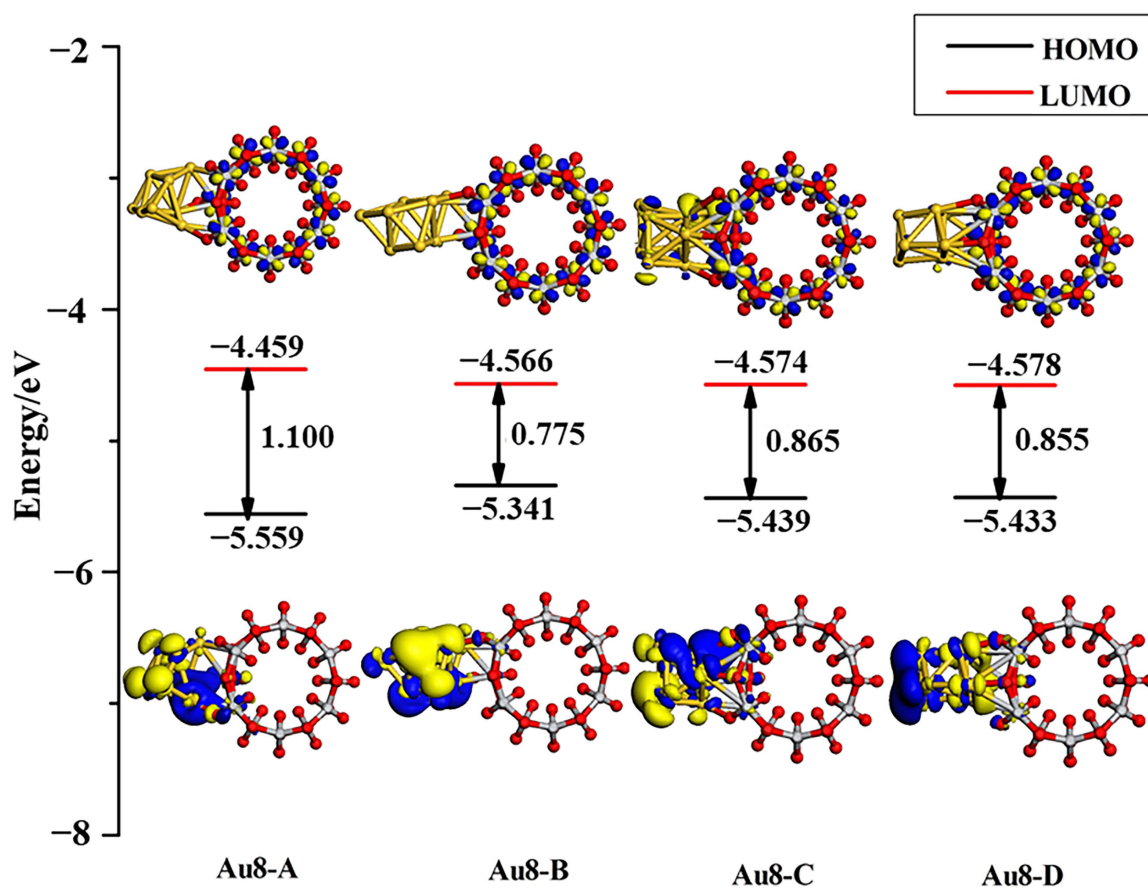

Figure 8. HOMO and LUMO along with the energy gap of four Au_8 adsorption systems calculated at the Γ-point. The isovalue set is 0.025 electrons/Å^3.

3.4. Structures of Au_{13}/TiO_2NT

Au_{13} clusters in the gas phase have two stable 3D arrangements: icosahedrons and cuboctahedrons. There is no energy barrier between these two configurations. In our study, the icosahedrons deformed into a distorted face-centered cubic structure after geometry optimization. Au_{13} clusters possessing the more stable configuration of cuboctahedrons

were selected to construct the Au_{13}/TiO_2NT system. Three stable adsorption configurations for Au_{13}/TiO_2NTs were obtained. The investigated configurations for the three adsorption systems are displayed in Figure 9. We can find that the condition of TiO_2NT surface oxygen atoms which bind with the cluster is similar to the $Au_{8-A(2cO,3cO,2cO)}$. For the $Au_{13-A(2cO,2cO)}$ configuration, in which the cluster is parallel to the TiO_2NT axial, Au_{13} bonded to two oxygen atoms on the nanotube surface and possessed the conformation with Au atoms spreading on the outside of nanotube surface, which is energetically preferred (see Table 3). In $Au_{13-B(2cO,3cO,2cO,3cO)}$, the absorbed Au_{13} cluster is similar to a cage-like structure [67,68], with four Au atoms directly bonding to the TiO_2NT surface. Since the cage-like structure covers less area of the TiO_2 nanotube than the flat geometry does, the density of the interfacial sites of the former is less than that of the latter. Although the cage-like structure is slightly less energetically favored than one of the geometries considered here, when the interface is considered as the controlling parameter, the cage-like Au_{13} nanoclusters can be expected to be more active than the other one for catalytic reactions. For optimized $Au_{13-C(3cO,2cO)}$ configuration, it also presents as a cage-like configuration. Au_{13} is adsorbed with a three-coordination oxygen atom and a two-coordination bridge oxygen atom, as shown in Figure 9C. The interaction of the Au_{13} with the nanotube surface was further analyzed with Mulliken charges. The adsorption energy for these structures and the Mulliken charges on the Au atoms and the binding atoms of TiO_2NT are summarized in Table 3. Au_{13}/TiO_2NT systems have greater adsorption energy than Au_8 and Au_1 systems (see Table 3). This indicates that increasing the number of Au atoms can enhance the stabilization of the adsorption system and the size scope of Au clusters according to the results of this study for the Au nanoclusters. According to Table 3, with previous Mulliken charge analysis results of Au_1 and Au_8, the Au_{13} clusters became negative after being absorbed on TiO_2NTs. However, the number of electrons transferred experiences no change. The interatomic charge distributions of related TiO_2NT surface atoms are shown in Table 3. The two main trends of atomic charge redistribution after the adsorption of Au_{13} clusters are: electron transfer to oxygen atoms and titanium losing electrons and showing a more positive charge, except for a few TiO_2NT surface atoms, which is similar to the Au_8 system. For further details, we integrated Mulliken charge analysis with deformation density (see Figure 5g,h); noticeably, there are significant electrons missing on the three coordination oxygen atoms, while the connected Au atoms obtain electrons, which are highlighted using a red dashed line in the EDD contour maps in Figure 5h.

Figure 10 shows the PDOS of Au_{13} clusters and connecting surface atoms of TiO_2NT along with the DOS of adsorption system. $5d$-Au has a contribution to the top of the valence band and overlaps well with the O $2p$ orbital for all three adsorption structures. With the electron density of $5d6s$-Au being raised, the contribution from Au atoms in the valence band and the conduction band was more and more obvious. The Au_{13} cluster adsorbed onto the TiO_2NT surface will have an excellent performance in electron transport. The HOMO and LUMO orbital diagrams of adsorption systems, as shown in Figure 11, visually illustrate the orbital analysis results given the density of states. Au_{13} nanoclusters contribute to the valence band and the conduction band, along with the increase in the number of gold atoms. HOMO and LUMO orbitals are mainly provided by the Au nanoclusters. Compared with the Au_8/TiO_2NT system, the system's energy is further decreased, particularly for the Au_{13-A} configuration, which downgraded the energy gap to 0.049 eV, far below the maximum energy value of the visible light absorption.
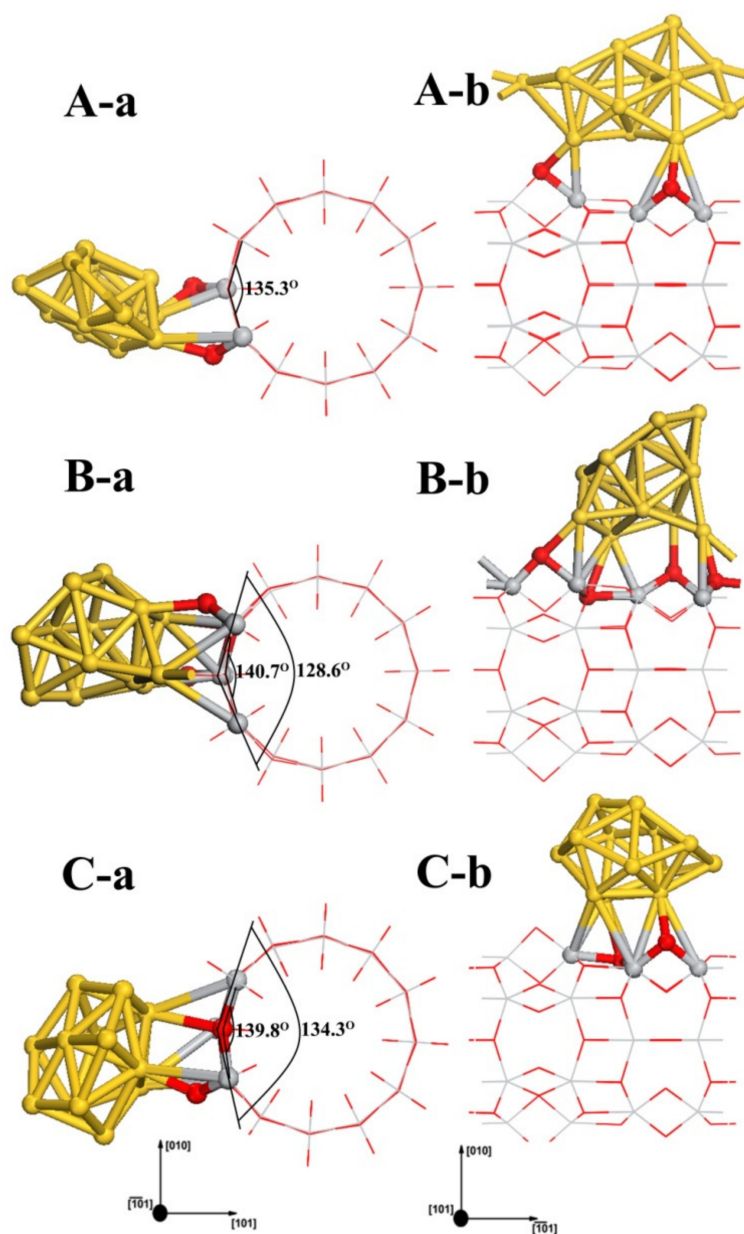
Figure 9. Four adsorption geometries for Au_{13} clusters on the TiO_2NT (6,0) are displayed as (**A–C**). (**a**,**b**) depict the cross-sectional view and the side view of the Au_{13} cluster absorption systems, respectively. The cross-sectional views of four adsorption geometries are shown as (**A-a**,**B-a**,**C-a**), respectively. The side vies of four adsorption geometries are shown as (**A-b**,**B-b**,**C-b**), respectively.

Table 3. Adsorption and clustering energies of Au_{13} and atomic Mulliken charges of Au and TiO_2NT surface atoms for the Au_{13}/TiO_2NT system in different configurations [a].

Configuration	Energy		Mulliken Charge (a.u.)												
	$E_{Au_{13}}^{ads}$ (eV)	$E_{Au_{13}}^{clu}$ (eV/atom)	Au_{13}	3cO [1]	2cO [1]	3cO [2]	2cO [2]	3cO [3]	2cO [3]	5cTi [1]	5cTi [2]	5cTi [3]	5cTi [4]	5cTi [5]	5cTi [6]
Bare TiO_2NT				−0.966	−0.779	−0.965	−0.779	−0.966	−0.779	1.717	1.714	1.718	1.714	1.713	1.717
Au_{13}-A(2cO,2cO)	3.12	2.28	−0.225		−0.870				−0.833	1.788	1.794			1.819	
Au_{13}-B(2cO,3cO,2cO,3cO)	2.23	2.21	−0.322	−0.996			−0.809	−0.929	−0.830	1.736		1.761	1.805	1.848	1.727
Au_{13}-C(3cO,2cO)	1.6	2.19	−0.171		−0.854	−0.934				1.762	1.791		1.737	1.778	

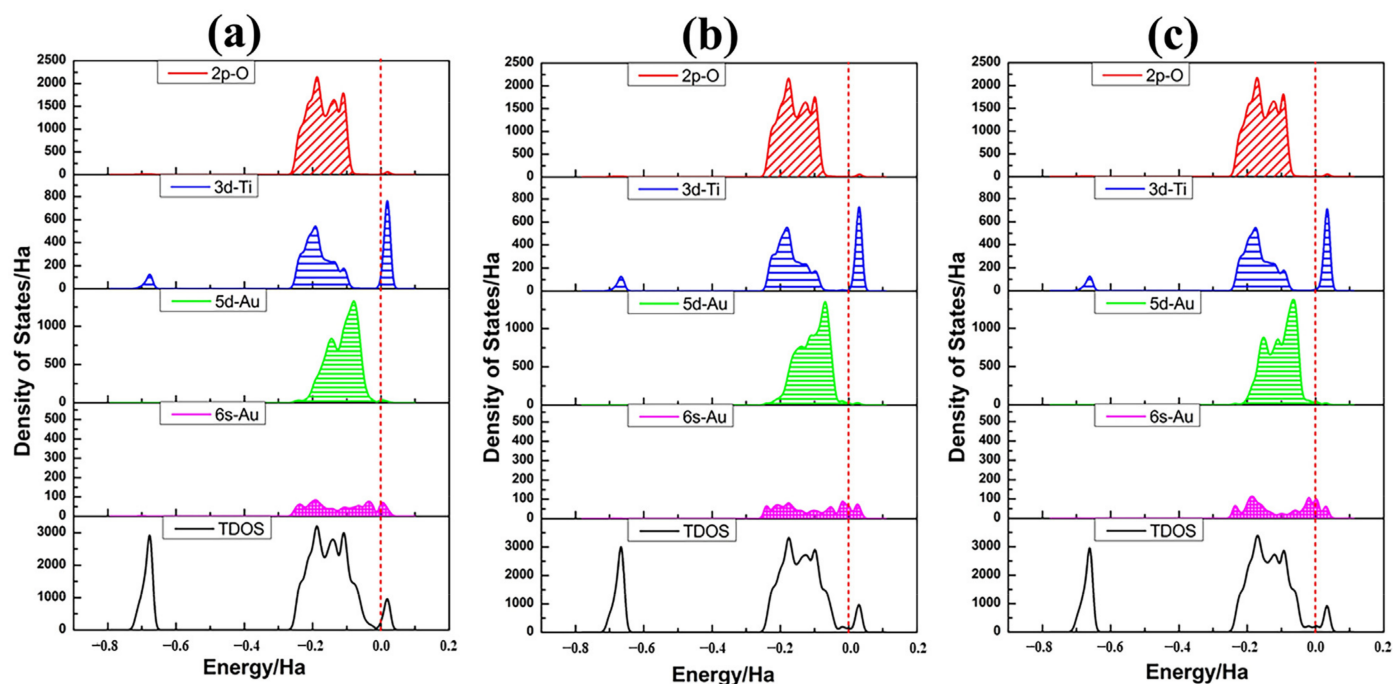[a] The superscripts on O and Ti indicate to which Au atom they are bound.

Figure 10. Density of state profiles and the partial density of states of Au$_{13}$ and relevant nanotube surface atoms for Au$_{13}$ clusters in four different adsorption states: (**a**) Au$_{13\text{-A}(2cO,2cO)}$, (**b**) Au$_{13\text{-B}(2cO,3cO,2cO,3cO)}$, (**c**) Au$_{13\text{-C}(3cO,2cO)}$. The detailed information is the same as in Figure 3.
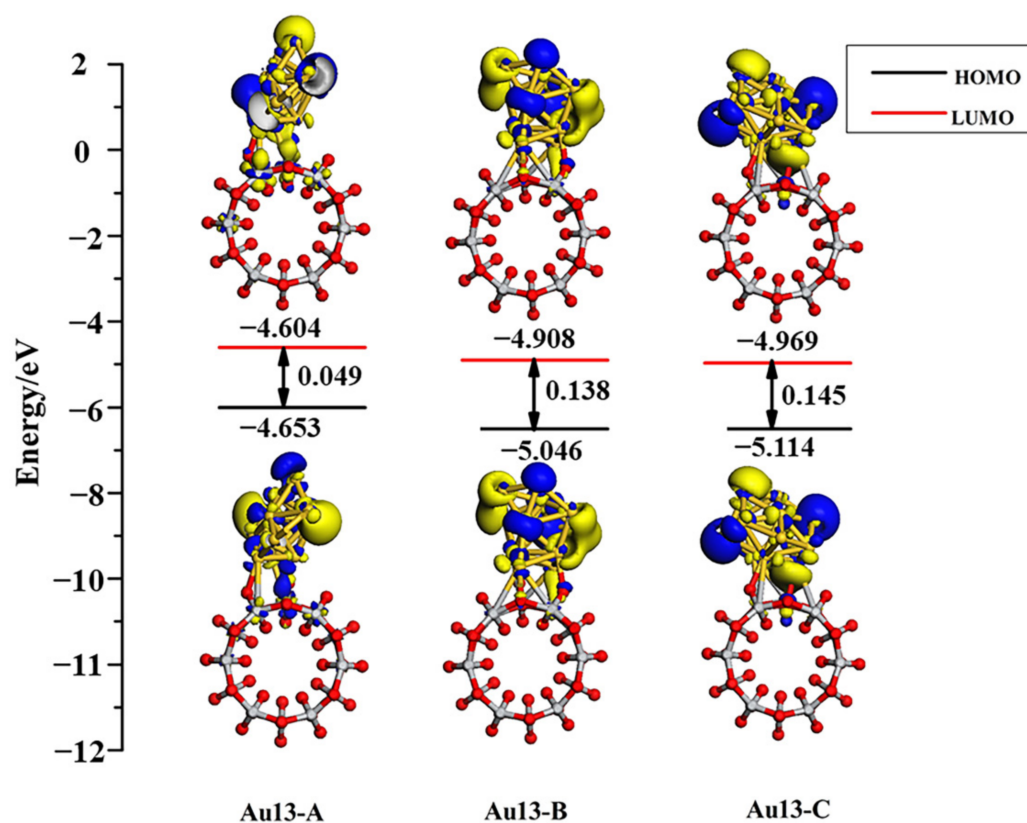

Figure 11. HOMO and LUMO along with the energy gap of four Au$_{13}$ adsorption systems calculated at the Γ-point. The isovalue set is 0.025 electrons/Å^3.

4. Conclusions

In summary, Au_n/TiO_2NTsystems are studied using density functional theory to characterize the effect of the adsorption of Au_n (n = 1, 8, 13) clusters on the geometric and electronic structures of anatase TiO_2NT. Our results show that a single Au adatom prefers the top position of 3cO as well as the bridging 2cO–2cO site of the TiO_2NT surface. Adsorbed Au_8 maintains a distorted biplanar configuration. The strong interaction between Au_n and atoms of the nanotube surface causes deformation of TiO_2NT. Au_{13} is adsorbed in a cage-like structure and has a tendency to spread out on the wetted nanotube surface.

The adsorption energy is increased as the number of Au atoms increases linearly, and increases in the size of Au_n clusters are conducive to stabilizing the load systems. The peaks at the Fermi level of the valence top and the conduction bottom come mainly from the contribution of $5d6s$-Au atoms. The $5d6s$ orbital of impurities' electronic state density caused valence widening and band gap narrowing. The band gap of the three most stable structures of adsorption systems Au_{1-A} (2.592 eV), Au_{8-A} (1.100 eV), and Au_{13-A} (0.049 eV) decreased compared to bare TiO_2NTs. This causes TiO_2NTs to achieve a visible light response. Molecular orbital diagrams intuitively verify the obviously increasing contribution to HOMO and LUMO orbitals with the increase in gold atoms. Our present results serve as a possible indicator that the nanojunction TiO_2NT/Au_n cluster, as a potential photoelectric device, possesses better energy and charge transmission performance.

References

1. Gong, X.B. Small Au and Pt Clusters at the Anatase TiO_2 (101) Surface: Behavior at Terraces, Steps, and Surface Oxygen Vacancies. *J. Am. Chem. Soc.* **2008**, *130*, 370–381. [CrossRef]
2. Han, Y.; Liu, C.; Ge, Q. Interaction of Pt Clusters with the Anatase TiO_2 (101) Surface: A First Principles Study. *J. Phys. Chem. B* **2006**, *110*, 7463–7472. [CrossRef] [PubMed]
3. Vittadini, A.; Selloni, A. Small Gold Clusters on Stoichiometric and Defected TiO_2 Anatase (101) and Their Interaction with CO: A Density Functional Study. *J. Chem. Phys.* **2002**, *117*, 353–361. [CrossRef]
4. Zhao, Q.; Li, M.; Chu, J.; Jiang, T.; Yin, H. Preparation, Characterization of Au (or Pt)-Loaded Titania Nanotubes and Their Photocatalytic Activities for Degradation of Methyl Orange. *Appl. Surf. Sci.* **2009**, *255*, 3773–3778. [CrossRef]
5. Goldman, N.; Browning, N.D. Gold Cluster Diffusion Kinetics on Stoichiometric and Reduced Surfaces of Rutile TiO_2(110). *J. Phys. Chem. C* **2011**, *115*, 11611–11617. [CrossRef]
6. Zhang, Z.; Tang, W.; Neurock, M.; Yates, J.T. Electric Charge of Single Au Atoms Adsorbed on TiO_2 (110) and Associated Band Bending. *J. Phys. Chem. C* **2011**, *115*, 23848–23853. [CrossRef]
7. Çakir, D.; Gülseren, O. Adsorption of Pt and Bimetallic PtAu Clusters on the Partially Reduced Rutile (110) TiO_2 Surface: A First-Principles Study. *J. Phys. Chem. C* **2012**, *116*, 5735–5746. [CrossRef]
8. Matthey, D.; Wang, J.G.; Wendt, S.; Matthiesen, J.; Schaub, R.; Lægsgaard, E.; Hammer, B.; Besenbacher, F. Enhanced Bonding of Gold Nanoparticles on Oxidized TiO_2 (110). *Science* **2007**, *315*, 1692–1696. [CrossRef]
9. Fu, C.; Li, M.; Li, H.; Li, C.; Wu, X.G.; Yang, B. Fabrication of Au Nanoparticle/TiO_2 Hybrid Films for Photoelectrocatalytic Degradation of Methyl Orange. *J. Alloys Compd.* **2017**, *692*, 727–733. [CrossRef]
10. Galeanoa, L.; Valencia, S.; Restrepo, G.; Marin, J.M. Dry-co-Grinding of Doped TiO_2 With Nitrogen, Silicon or Selenium for Enhanced Photocatalytic Activity under UV/Visible and Visible Light Irradiation for Environmental Applications. *Mater. Sci. Semicond. Process.* **2019**, *91*, 47–57. [CrossRef]

11. Maolanon, R.; Wongwiriyapan, W.; Pratontep, S. TiO$_2$/Pt/TiO$_2$ Sandwich Nanostructures: Towards Alcohol Sensing and UV Irradiation-Assisted Recovery. *J. Chem.* **2017**, *2017*, 8545690. [CrossRef]

12. Saeed, K.; Khan, I.; Gul, T.; Sadiq, M. Efficient Photodegradation of Methyl Violet Dye Using TiO$_2$/Pt and TiO$_2$/Pdphotocatalysts. *Appl. Water Sci.* **2017**, *7*, 3841–3848. [CrossRef]

13. Pan, X.; Chen, X.; Yi, Z. Defective, Porous TiO$_2$ Nanosheets with Pt Decoration as an Efficient Photocatalyst for Ethylene Oxidation Synthesized by a C$_3$N$_4$ Templating Method. *ACS Appl. Mater. Interfaces* **2016**, *8*, 10104–10108. [CrossRef]

14. Maeda, K.; Domen, K. Photocatalytic Water Splitting: Recent Progress and Future Challenges. *J. Phys. Chem. Lett.* **2010**, *1*, 2655–2661. [CrossRef]

15. Teoh, W.Y.; Scott, J.A.; Amal, R. Progress in Heterogeneous Photocatalysis: From Classical Radical Chemistry to Engineering Nanomaterials and Solar Reactors. *J. Phys. Chem. Lett.* **2012**, *3*, 629–639. [CrossRef]

16. Miyasaka, T. Toward Printable Sensitized Mesoscopic Solar Cells: Light-Harvesting Management with Thin TiO$_2$ Films. *J. Phys. Chem. Lett.* **2011**, *2*, 262–269. [CrossRef]

17. Mora-Seró, I.; Bisquert, J. Breakthroughs in the Development of Semiconductor-Sensitized Solar Cells. *J. Phys. Chem. Lett.* **2010**, *1*, 3046–3052. [CrossRef]

18. Braga, A.; Giménez, S.; Concina, I.; Vomiero, A.; Mora-Seró, I. Panchromatic Sensitized Solar Cells Based on Metal Sulfide Quantum Dots Grown Directly on Nanostructured TiO$_2$ Electrodes. *J. Phys. Chem. Lett.* **2011**, *2*, 454–460. [CrossRef]

19. Mowbray, D.J.; Martínez, J.I.; Calle-Vallejo, F.; Rossmeisl, J.; Thygesen, K.S.; Jacobsen, K.W.; Nørskov, J.K. Trends in Metal Oxide Stability for Nanorods, Nanotubes, and Surfaces. *J. Phys. Chem. C* **2011**, *115*, 2244–2252. [CrossRef]

20. Yu, J.G.; Hai, Y.; Cheng, B. Enhanced Photocatalytic H$_2$-Production Activity of TiO$_2$ by Ni(OH)$_2$ Cluster Modification. *J. Phys. Chem. C* **2011**, *115*, 4953–4958. [CrossRef]

21. Petrik, N.G.; Kimmel, G.A. Electron-and Hole-Mediated Reactions in UV-Irradiated O$_2$ Adsorbed on Reduced Rutile TiO$_2$ (110). *J. Phys. Chem. C* **2011**, *115*, 152–164. [CrossRef]

22. Chrétien, S.; Metiu, H. Electronic Structure of Partially Reduced Rutile TiO$_2$ (110) Surface: Where Are the Unpaired Electrons Located? *J. Phys. Chem. C* **2011**, *115*, 4696–4705. [CrossRef]

23. Deskins, N.A.; Rousseau, R.; Dupuis, M. Defining the Role of Excess Electrons in the Surface Chemistry of TiO$_2$. *J. Phys. Chem. C* **2010**, *114*, 5891–5897. [CrossRef]

24. Asahi, R.; Taga, Y.; Mannstadt, W.; Freeman, A.J. Electronic and Optical Properties of Anatase TiO$_2$. *Phys. Rev. B* **2000**, *6*, 7459–7465. [CrossRef]

25. Tang, H.; Berger, H.; Schmid, P.E.; Lévy, F. Photoluminescence in TiO$_2$ Anatase Single Crystals. *Solid State Commun.* **1993**, *87*, 847–850. [CrossRef]

26. Pu, Y.C.; Wang, G.; Chang, K.D.; Ling, Y.; Lin, Y.K.; Fitzmorris, B.C.; Liu, C.M.; Lu, X.; Tong, Y.; Zhang, J.Z.; et al. Au Nanostructure-Decorated TiO$_2$ Nanowires Exhibiting Photoactivity across Entire UV-visible Region for Photoelectrochemical Water Splitting. *Nano Lett.* **2013**, *13*, 3817–3823. [CrossRef] [PubMed]

27. Malato, S.; Fernández-Ibáñez, P.; Maldonado, M.I.; Blanco, J.; Gernjak, W. Decontamination and Disinfection of Water by Solar Photocatalysis. Recent Overview and Trends. *Catal. Today* **2009**, *147*, 1–59. [CrossRef]

28. Leary, R.; Westwood, A. Carbonaceous Nanomaterials for the Enhancement of TiO$_2$ Photocatalysis. *Carbon* **2011**, *49*, 741–772. [CrossRef]

29. Gao, L.D.; Le, Y.; Wang, J.X.; Chen, J.F. Preparation and Characterization of Titanium Nanotubes with Mesostructured Walls. *Mater. Lett.* **2006**, *60*, 3882–3886. [CrossRef]

30. Nunzi, F.; Angelis, F.D. DFT Investigations of Formic Acid Adsorption on Single-Wall TiO$_2$ Nanotubes: Effect of the Surface Curvature. *J. Phys. Chem. C* **2011**, *115*, 2179–2186. [CrossRef]

31. Shankar, K.; Bandara, J.; Paulose, M.; Wietasch, H.; Varghese, O.K.; Mor, G.K.; LaTempa, T.J.; Thelakkat, M.; Grimes, C.A. Highly Efficient Solar Cells using TiO$_2$ Nanotube Arrays Sensitized with a Donor-Antenna Dye. *Nano Lett.* **2008**, *8*, 1654–1659. [CrossRef]

32. Macak, J.M.; Zlamal, M.; Krysa, J.; Schmuki, P. Self-Organized TiO$_2$ Nanotube Layers as Highly Efficient Photocatalysts. *Nano Micro Small* **2007**, *3*, 300–304. [CrossRef]

33. Kuang, D.; Brillet, J.R.M.; Chen, P.; Takata, M.; Uchida, S.; Miura, H.; Sumioka, K.; Zakeeruddin, S.M.; Grätzel, M. Application of Highly Ordered TiO$_2$ Nanotube Arrays in Flexible Dye-Sensitized Solar Cells. *ACS Nano* **2008**, *2*, 1113–1116. [CrossRef]

34. Hossain, F.M.; Evteev, A.V.; Belova, I.V.; Nowotny, J.; Murch, G.E. Electronic and Optical Properties of Anatase TiO$_2$ Nanotubes. *Comput. Mater. Sci.* **2010**, *48*, 854–858. [CrossRef]

35. Chen, H.M.; Chen, C.K.; Chang, Y.C.; Tsai, C.W.; Liu, R.S.; Hu, S.F.; Chang, W.S.; Chen, K.H. Quantum Dot Monolayer Sensitized ZnO Nanowire-Array Photoelectrodes: True Efficiency for Water Splitting. *Angew. Chem. Int. Ed.* **2010**, *49*, 5966–5969. [CrossRef]

36. Lee, Y.L.; Chi, C.F.; Liau, S.Y. CdS/CdSe Co-Sensitized TiO$_2$ Photoelectrode for Efficient Hydrogen Generation in a Photoelectro-chemical Cell. *Chem. Mater.* **2010**, *22*, 922–927. [CrossRef]

37. Gao, Z.D.; Liu, H.F.; Li, C.Y.; Song, Y.Y. Biotemplated Synthesis of Au Nanoparticles–TiO$_2$ Nanotube Junctions for Enhanced Direct Electrochemistry of Heme Proteins. *Chem. Commun.* **2013**, *49*, 774–776. [CrossRef]

38. Shao, Z.; Wang, X.; Ren, S.; Tian, Z.; Fan, S.; Sun, S.; Liu, S.; Wang, Q. Improved Visible Solar Absorber Based on TiO$_2$ Nanotube Film by Surface-Loading of Plasmonic Au Nanoparticles. *J. Appl. Phys.* **2013**, *114*, 063510. [CrossRef]

39. Chen, S.; Malig, M.; Tian, M.; Chen, A. Electrocatalytic Activity of PtAu Nanoparticles Deposited on TiO$_2$ Nanotubes. *J. Phys. Chem. C* **2012**, *116*, 3298–3304. [CrossRef]

40.   Bao, H.H. Microwave Synthesis and Charaterization of Ag, Au, Pt nanoparticles Supported on TiO$_2$ Nanotubes. *Chin. J. Inorg. Chem.* **2005**, *21*, 374–378.

41.   Xiao, F. An Efficient Layer-by-Layer Self-Assembly of Metal-TiO$_2$ Nanoring/Nanotube Heterostructures, M/T-NRNT (M = Au, Ag, Pt), for Versatile Catalytic Applications. *Chem. Commun.* **2012**, *48*, 6538–6540. [CrossRef]

42.   Zhu, B.L.; Guo, Q.; Wang, S.; Zheng, X.; Zhang, S.; Wu, S.; Huang, W. Synthesis of MetalDdoped TiO$_2$ Nanotubes and Their Catalytic Performance for Low-Temperature CO Oxidation. *React. Kinet. Catal. Lett.* **2006**, *88*, 301–308. [CrossRef]

43.   Chen, X.; Liu, W.; Tang, L.; Wang, J.; Pan, H.; Du, M. Electrochemical Sensor for Detection of Hydrazine Based on Au@Pd Core–Shell Nanoparticles Supported on Amino-Functionalized TiO$_2$ Nanotubes. *Mater. Sci. Eng. C* **2014**, *34*, 304–310. [CrossRef] [PubMed]

44.   Yu, J.; Xiang, Q.; Zhou, M. Preparation, Characterization and Visible-Light-Driven Photocatalytic Activity of Fe-Doped Titani-ananorods and First-Principles Study for Electronic Structures. *App. Catal. B Environ.* **2009**, *90*, 595–602. [CrossRef]

45.   Diebold, U. The Surface Science of Titanium Dioxide. *Surf. Sci. Rep.* **2003**, *48*, 53–229. [CrossRef]

46.   Diebold, U.; Lehman, J.; Mahmoud, T.; Kuhn, M.; Leonardelli, G.; Hebenstreit, W.; Schmid, M.; Varga, P. Intrinsic Defects on a TiO$_2$ (110)(1×1) Surface and Their Reaction with Oxygen: A Scanning Tunneling Microscopy Study. *Surf. Sci.* **1998**, *411*, 137–153. [CrossRef]

47.   Hengerer, R.; Bolliger, B.; Erbudak, M.; Gratzel, M. Structure and Stability of the Anatase TiO$_2$ (101) and (001) Surfaces. *Surf. Sci.* **2000**, *460*, 162–169. [CrossRef]

48.   Lazzeri, M.; Vittadini, A.; Selloni, A. Structure and Energetics of Stoichiometric TiO$_2$ Anatase Surfaces. *Phys. Rev. B* **2001**, *63*, 155409. [CrossRef]

49.   Haruta, M. When Gold Is Not Noble: Catalysis by Nanoparticles. *Chem. Rec.* **2003**, *3*, 75–87. [CrossRef]

50.   De Sekhar, H.; Krishnamurty, S.; Sourav, P. Understanding the Reactivity Properties of Au$_n$ ($6 \leq n \leq 13$) Clusters Using Density Functional Theory Based Reactivity Descriptors. *J. Phys. Chem. C* **2010**, *114*, 6690–6703. [CrossRef]

51.   Sanchez, A.; Abbet, S.; Heiz, U.; Schneider, W.D.; Häkkinen, H.; Barnett, R.N.; Landman, U. When Gold Is Not Noble: Nanoscale Gold Catalysts. *J. Phys. Chem. A* **1999**, *103*, 9573–9578. [CrossRef]

52.   Häkkinen, H.; Abbet, S.; Sanchez, A.; Heiz, U.; Landman, U. Structural, Electronic, and Impurity-Doping Effects in Nanoscale Chemistry: Supported Gold Nanoclusters. *Angew. Chem. Int. Ed.* **2003**, *42*, 1297–1300. [CrossRef]

53.   Yoon, B.; Häkkinen, H.; Landman, U.; Wörz, A.S.; Antonietti, J.M.; Abbet, S.; Judai, K.; Heiz, U. Charging Effects on Bonding and Catalyzed Oxidation of CO on Au$_8$ Clusters on MgO. *Science* **2005**, *307*, 403–407. [CrossRef]

54.   Fernández, E.M.; Soler, J.M.; Garzón, I.L.; Balbás, L.C. Trends in the Structure and Bonding of Noble Metal Clusters. *Phys. Rev. B* **2004**, *70*, 165403. [CrossRef]

55.   Oviedo, J.; Palmer, R.E. Amorphous Structures of Cu, Ag, and Au Nanoclusters from First Principles Calculations. *J. Chem. Phys.* **2002**, *117*, 9548–9551. [CrossRef]

56.   Chang, C.M.; Chou, M.Y. Alternative Low-Symmetry Structure for 13-Atom Metal Clusters. *Phys. Rev. Lett.* **2004**, *93*, 133401–133404. [CrossRef]

57.   Shafai, G.; Hong, S.; Bertino, M.; Rahman, T.S. Effect of Ligands on the Geometric and Electronic Structure of Au$_{13}$ Clusters. *J. Phys. Chem. C* **2009**, *113*, 12072–12078. [CrossRef]

58.   Perdew, J.P.; Burke, K.; Ernzerhof, M. Generalized Gradient Approximation Made Simple. *Phys. Rev. Lett.* **1996**, *77*, 3865–3868. [CrossRef]

59.   Delley, B. An Allelectron Numerical Method for Solving the Local Density Functional Forpolyatomic Molecules. *J. Chem. Phys.* **1990**, *92*, 508–517. [CrossRef]

60.   Delley, B. From Molecules to Solids with the DMol3 Approach. *J. Chem. Phys.* **2000**, *113*, 7756–7764. [CrossRef]

61.   Dong, C.; Li, X.; Qi, J. First-Principles Investigation on Electronic Properties of Quantum Dot-Sensitized Solar Cells Based on Anatase TiO$_2$ Nanotubes. *J. Phys. Chem. C* **2011**, *115*, 20307–20315. [CrossRef]

62.   Monkhorst, H.J.; Pack, J.D. Special Points for Brillouin-Zone Integrations. *Phys. Rev. B* **1976**, *13*, 5188–5192. [CrossRef]

63.   Burdett, J.K.; Hughbanks, T.; Miller, G.J.; Richardson, J.W., Jr.; Smith, V. Structural-Electronic Relationships in Inorganic Solids: Powder Neutron Diffraction Studies of the Rutile and Anatase Polymorphs of Titanium Dioxide at 15 and 295 K. *J. Am. Chem. Soc.* **1987**, *109*, 3639–3646. [CrossRef]

64.   Evarestov, R.A.; Zhukovskii, Y.F.; Bandura, A.V.; Piskunov, S. Symmetry and Models of Single-Walled TiO$_2$ Nanotubes with Rectangular Morphology. *Cent. Eur. J. Phys.* **2011**, *9*, 492–501. [CrossRef]

65.   Bandura, A.V.; Evarestov, R.A. From Anatase (101) Surface to TiO$_2$ Nanotubes: Rolling Procedure and First Principles LCAO Calculations. *Surf. Sci.* **2009**, *603*, 117–120. [CrossRef]

66.   Cho, Y.; Kim, C.; Moon, H.; Choi, Y.; Park, S.; Lee, C.-K.; Han, S. Electronic Structure Tailoring and Selective Adsorption Mechanism of Metal-coated Nanotubes. *Nano Lett.* **2008**, *8*, 81–86. [CrossRef] [PubMed]

67.   Dong, Y.; Springborg, M. Global Structure Optimization Study on Au2–20. *Eur. Phys. J. D* **2007**, *43*, 15–18. [CrossRef]

68.   Hong, S.; Rahman, T.S. Rationale for the Higher Reactivity of Interfacial Sites in Methanol Decomposition on Au$_{13}$/TiO$_2$(110). *J. Am. Chem. Soc.* **2013**, *135*, 7629–7635. [CrossRef]